Geophysical Journal International

Geophys. J. Int. (2021) **227,** 544–558
Advance Access publication 2021 June 21
GJI Seismology

https://doi.org/10.1093/gji/ggab235

3-D Q-coda attenuation structure at Mt Etna (Italy)

E. Giampiccolo,[1] E. Del Pezzo,[2,3] T. Tuvé,[1] G. Di Grazia[1] and J.M. Ibáñez[1,3]

[1]*Istituto Nazionale di Geofisica e Vulcanologia, Osservatorio Etneo, Piazza Roma 2, Catania, Italy. E-mail: edoardo.delpezzo@ingv.it*
[2]*Istituto Nazionale di Geofisica e Vulcanologia, Osservatorio Vesuviano, via Diocleziano 328, Napoli, Italy*
[3]*Instituto Andaluz de Geofisica, University of Granada, Granada, Spain*

Accepted 2021 June 16. Received 2021 June 8; in original form 2021 January 29

SUMMARY

Three dimensional attenuation images of Mt Etna volcano obtained by the analysis of *Q*-coda from local volcano-tectonic earthquakes are presented in this work. Seismic sources are confined inside the Etna structure with a maximum focal depth of 35 km below the sea level. The space distribution of the attenuation values was calculated by using 3-D weighting functions derived by the sensitivity kernels of Pacheco & Snieders and approximated by a polynomial interpolation, represented in the maps by using a backprojection method. Data were analyzed in four bands with central frequency placed at 1.5, 3, 6 and 12 Hz, respectively. We observed a frequency dependence of *Q*-coda with values that range from 55 at 1.5 Hz to 218 at 12 Hz. *Q*-coda space distribution in the Etna area shows almost uniformity in the average attenuation in the first 35 km below the surface. The images were derived with a resolution of 5 km. We observe as one of our main conclusions that *Q*-coda attenuation space anomalies are correlated with the areas of highest structural heterogeneities and are distributed along the well-known tectonic structures which characterize the crust in Mt Etna region. Previous and numerous velocity and attenuation images describing the structure of Mt Etna support our main conclusion: high *Q*-coda volumes almost coincide with the zones marked by high velocity and relative low total attenuation for direct waves.

Key words: Coda waves; Seismic attenuation; Seismic tomography; Wave scattering and diffraction.

1 INTRODUCTION

The investigation of the crust and upper mantle structure of Mt Etna volcano has been a big challenge for the volcanological community for many decades (Cassinis *et al.* 1969; Sharp *et al.* 1980; Hirn *et al.* 1991; Cardaci *et al.* 1993; Hirn *et al.* 1997). From the year 2000 up to the present, seismological studies, accompanied by the progressive enhancement in instruments and methods, contributed with new observations and models to improve the knowledge of the geological structure of this volcanic region. For instance, tomographic studies provided new 3-D velocity images of this area improving number and quality of the structural models (Chiarabba *et al.* 2000, 2004; Laigle *et al.* 2000; Aloisi *et al.* 2002; Patanè *et al.* 2002, 2006; De Gori *et al.* 2011b; Alparone *et al.* 2012; Dìaz-Moreno *et al.* 2018; Giampiccolo *et al.* 2020). All these works provided an increasing number of details showing low- and high-velocity anomalies depicting lateral discontinuities and evidencing the structural complexity of this volcanic area.

Since the attenuation of *P* and *S* waves provides important additional information on the Earth structure, because of its sensitivity to rock composition, fluid content, temperature and other properties, it turns out that it is a necessary information to complement the velocity imaging. The attenuation images permit in facts a more complete structural interpretation and become crucial in volcanoes, where high temperature, hot fluids, partial melting and heterogeneity of the geological structures strongly affect the rock properties.

It is well known that the attenuation mechanism depends on one hand on the existence of significant heterogeneity, on the other hand on the presence of molten materials as magma lens or bodies. This leads to a wide variety of examples that associate different volcanic structures (rigid, cooled and molten) with geological conditions (e.g. Del Pezzo 2008; Sato *et al.* 2012). In this sense, Mt Etna volcano is the ideal target to perform studies on attenuation imaging (De Gori *et al.* 2005; Martinez-Arevalo *et al.* 2005; De Gori *et al.* 2011a; Alparone *et al.* 2012; Ibáñez *et al.* 2020). It is noteworthy that all the above mentioned works have evidenced the absence of a clear high attenuation anomaly in the crust that could be interpretable as melt accumulation and therefore as a possible magma chamber in the crust. Conversely, the combination of velocity and attenuation studies has evidenced the existence of strong lateral anomalies interpreted as a broad complex of intrusive bodies, placed in the middle and upper crust, that explain the feeding mechanism of the volcanic system. (e.g. Patanè *et al.* 2011).

Mt Etna is an ideal location to develop any type of tomographic studies thanks to the large local earthquake data set available. Since the local earthquakes beneath the volcano (Fig. 1) occurring in such heterogeneous medium generate high energy diffusive- (or scattering-) wave fields (the coda waves), scattering tomography is easily applicable. The images produced using this approach turn out to be complementary to the already obtained tomography images in velocity and attenuation, both for P and S waves (see e.g., Larose *et al.* 2010, and references therein). Among the different methods based on the analysis of the diffusive wave field, the Coda wave interferometry (Snieder 2006) is used to monitor variations of the elastic properties of the Earth medium, while the coda waves imaging (Mayor *et al.* 2016; Prudencio *et al.* 2013a) yields pictures of the scattering and of intrinsic attenuation space distribution. Crucial in these last approaches is the use of the sensitivity kernels of the scattering wave field. Their estimation is based on the 'average local time', concept that is defined as the time in which the elastic wave energy pass through a small volume of Earth located at a given space position (Obermann *et al.* 2013). The sensitivity kernels are thus space–time functions describing the space–time distribution of seismic energy. They, in other words, describe where and when in the Earth medium the seismic radiation composing the coda of the local earthquakes is generated. For this reason the sensitivity kernels are extremely important to associate the attenuation parameter(s) derived by the analysis of seismic coda with a particular zone inside the earth medium, allowing the construction of an attenuation image. Recently, sensitivity kernels for scattering radiation have been used to depict 2-D and 3-D volcanic structures (see for example the works of De Siena *et al.* 2013; Prudencio *et al.* 2013a, b, 2015; Del Pezzo *et al.* 2016; De Siena *et al.* 2016) or to study tectonically active zones (e.g. Mayor *et al.* 2016; Sketsiou *et al.* 2020). In this paper, we obtained a 3-D Q-coda tomography for Mt Etna using a projection method based on the use of weighting functions derived from the sensitivity kernels calculated by Pacheco & Snieder (2006), and compared the results obtained with some of the previous seismological (mainly in velocity) images of this volcano. In addition, we studied the correspondence of the present results with a recent 2-D structure of the shallow part of Etna based on the joint measurements of intrinsic- and scattering-attenuation (Ibáñez *et al.* 2020), carried out using passive and active data sets. The present Q-coda tomography reproduces the S-wave attenuation structure for this volcano down to a depth of 35 km in four frequency bands centered at 1.5, 3, 6 and 12 Hz, respectively. We will show how our present images evidence that the strongest attenuation contrasts are well correlated with the local geotectonic setting, and with the pattern of the main faults and fractures characterizing the crust at Mt Etna. In addition, the observed correspondence of the present results with those from previous studies confirms the value of the technique as a complementary tool to be combined with the tomographic images of the velocity structure.

2 STRUCTURAL AND SEISMOLOGICAL SETTING OF THE MT ETNA AREA

Mt Etna volcano (Fig. 1) is one of the best European volcanic laboratories and its associated natural seismicity is ideal to study the deep structure beneath an active volcano. It is a 3300 m high polygenetic volcano, placed on the eastern coast of Sicily in front of the Apennine–Maghrebian collision belt (Lentini 1982). In the literature is possible to find several works that describe many structural aspects of the volcanic environment (De Guidi *et al.* 2014). However, the complex tectonic and geodynamic setting is still under study, with a broad set of hypotheses interpreting its origin and evolution (i.e. Rittmann 1973; Continisio *et al.* 1997; Hirn *et al.* 1997; Tanguy *et al.* 1997; Gvirtzman & Nur 1999; Faccenna *et al.* 2001; Clocchiatti *et al.* 2004). The the N–S compression, active in northern Sicily, dominates the regional deformation (Bousquet & Lanzafame 2004) that is contemporaneously active with an E–W extension, active on the eastern side, and with a right-lateral transtension both offshore along the Malta Escarpment Fault System (MEFS; Fig.1) and onshore along the Timpe Fault System (TFS; Fig. 1) and with set of parallel normal faults striking from NNW to NW (Azzaro *et al.* 2012). In particular, the important zones of Valle del Bove (VdB) and the volcano-tectonic structures of the NE Rift (Fig. 1) placed in the eastern flank of the volcano are separated from the Ioanian Coast by the Pernicana Fault (PF) and by the Timpe Fault System, which are considered the most important tectonic elements at Mt Etna (see Azzaro *et al.* 2012, 2013, 2017) controlling the ESE seaward displacement of the eastern flank as indicated by numerous studies (e.g. Borgia *et al.* 1992; Lo Giudice *et al.* 1992; Rust & Neri 1996; Bonforte & Puglisi 2003; Rust *et al.* 2005; Branca & Ferrara 2013; Urlaub *et al.* 2018, among others). The seismicity of Mt Etna is mainly characterized by crustal shallow ($<$10 km depth) volcano-tectonic earthquakes (VT), related to the seismic activity of the already described fault systems and to the volcano induced stress dynamics generating seismic activity (e.g., Patanè *et al.* 2004; Solaro *et al.* 2010). The most intense seismic activity occurs in the eastern flank of the volcano, associated with the Timpe Fault System and the Pernicana Fault. The latter fault system is composed by few active tectonic structures mainly aligned with the E–W direction, showing a peculiar seismic pattern, as evidenced by the above cited authors. Other structures are the N–S trending Ragalna Fault System (RFS) and the NW–SE Trecastagni and Tremestieri faults (TCF; TMF) in the South (Alparone *et al.* 2013; Azzaro *et al.* 2013,and references therein). These structures generate frequent moderate magnitude earthquakes which historically caused destruction or severe damage in the villages and cities of the area. Intermediate ($10 < h < 15$ km) and deep ($15 < h < 35$ km) earthquakes, occurring beneath the western flank of the volcano (Fig. 1) in some cases have been associated with episodic movements of magmatic batches from depth toward the surface (e.g. Musumeci *et al.* 2004; Alparone *et al.* 2012; Mostaccio *et al.* 2013). In the deep crust (between 22 and 30 km of depth) beneath the north-western area of Mt Etna volcano is placed one of the most significant deep seismo-genic volumes (Azzaro *et al.* 2017). However, this seismicity is at the present interpreted on the base of tectonic regional dynamics associated with the well-known compressive regime at the front of the Sicilian Chain-Foreland (Lavecchia *et al.* 2007; Scarfì *et al.* 2016). In addition, local VT seismicity associated with deformation processes (inflation-deflation) of the volcanic edifice, ground fracturing due to magma injection in shallow dike systems and other processes related to the Mt Etna dynamics are observed in the summit region. Other sources of deformation in the Mt Etna edifice are associated with the morphological conditions related to flank gravitational instability or to regional normal-oblique faulting (Azzaro *et al.* 2013). Finally, important is also the presence of underground water reservoir beneath Mt Etna to understand the observed seismic behavior. Federico *et al.* (2017) show that Mt Etna is characterized by discontinuous low-permeability pyroclastic layers interbedded in highly permeable lavas. The additional existence

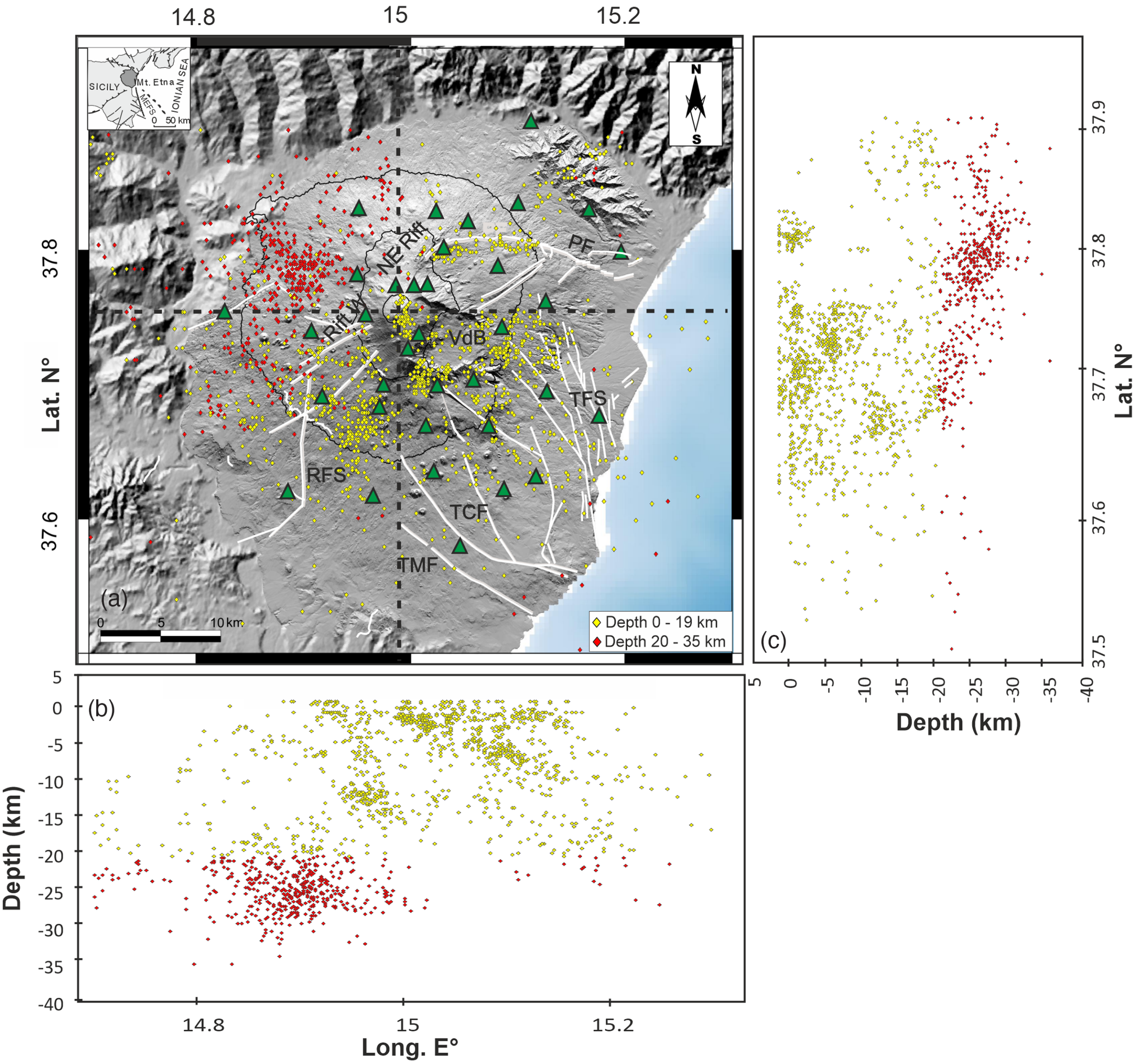

Figure 1. Map of the Etna area. Green triangles represents the receiver locations. Red dots mark the deepest, (upper mantle), while yellow dots the shallowest (crust) earthquake sources. White lines depict the Etna faults. Black dotted lines are the profiles of cross sections shown in Fig. 6. In the inset, dashed lines depict the regional fault structures. (b) Hypocentres projected in a E–W section. (c) Hypocentres projected in a N–S section.

in the region of an impermeable substratum creates an important groundwater reservoir beneath Mt Etna structure. The impermeable sedimentary basement morphology controls the confined deep water circulation. Since the basement of Mt Etna has its highest elevation (about 1300 m a.s.l.), placed a few kilometres towards northwest of the volcano summit and dipping toward the southeast, groundwater tends to move and accumulate in the eastern and southern flanks of the volcano (Ogniben 1966; Branca & Ferrara 2013)

3 THEORY, METHODS AND DATA PROCESSING

3.1 *Q*-coda

The total-Q or Q_t, the total quality factor for seismic waves, can be expressed as

$$Q_i^{-1} + Q_s^{-1} = Q_t^{-1},$$

where Q_i is the intrinsic-Q, accounting for the Energy transformed in heat during the propagation and Q_s is the scattering-Q, accounting for the primary wave Energy lost by scattering from the medium heterogeneities and recovered in the seismic coda of the local earthquakes.

Q-coda, hereafter Q_c, is the parameter describing the time decay of the seismogram coda energy envelope. Assuming 3-D body wave propagation in a half space with constant velocity

$$E(\omega, t) \propto \frac{E_0}{t^2} \exp\left(-\frac{\omega t}{Q_c}\right), \tag{1}$$

where $E(\omega, t)$ represents the short period local or regional seismogram energy envelope, E_0 is the source energy, ω is the angular frequency, t is the time elapsed since the origin time of the earthquake. Aki & Chouet (1975) showed that eq. (1) corresponds to the Single Scattering model in case of colocated source and receiver, and interpreted Q_c as the total-Q for S waves. Since the appearance in literature of this pioneering paper, a large number of Q-coda estimates were carried out in the world, with the main purpose of estimating Q_t. Sato (1977) introduced the source-receiver distance, r, and reformulated the single-scattering model as

$$E(\omega, r, t) = \frac{E_0 g_0}{4\pi r^2} K\left(\frac{vt}{r}\right) H(vt - r) \exp\left(-\frac{\omega t}{Q_c}\right), \tag{2}$$

where g_0 is called 'scattering coefficient', the inverse of the mean free path, l_0, v is the S-wave speed, H represents the Heaviside function and $K(x) = \frac{1}{x} ln(\frac{x+1}{x-1})$.

It was later demonstrated (Zeng *et al.* 1991) that the eq. (2) is the first order approximation, strictly valid only for large l_0, of the 3-D solution of the general energy transport integral equation. A solution of this last equation, accounting for multiple scattering, was found by Paasschens (1997) with an interpolation procedure. Unfortunately, the conditions for the application of the single scattering assumption in the real Earth are far from being realistic, and in most experimental works the estimate of attenuation carried out measuring Q_c is biased due to the underlaying assumption of half space with constant velocity. In such studies it emerges that Q_c, for most of the study areas, is a measure of Q_i and not of Q_t for S waves, as was assumed in the early applications, and that the absolute value of Q is generally underestimated due to the unrealistic assumption of half-space. This clearly emerges from attenuation studies based on the Multiple LApse Time WindowAnalysis (MLTWA) technique (see e.g. Mayeda *et al.* 1992; Sato *et al.* 2012; Del Pezzo & Ibáñez 2020, for a review) and successive studies which resolve the trade-off between Q_i and Q_s by integrating the energy associated with the ballistic waves (Gaebler *et al.* 2015; Eulenfeld & Wegler 2016, 2017). In these studies, the solution of the general transport equation (see e.g. Margerin 2011, for a review) is applied to jointly retrieve Q_i and Q_s . The measure of Q_c has been found to depend on the time interval selected for coda analysis, generally starting the analysis at twice the S-wave traveltime and ending at 60–100 s after the origin time, depending on the earthquake magnitude and experimental conditions (Sato *et al.* 2012). This happens due to the improper application of eq. (2) to the cases where the single scattering approximation is unrealistic. In such cases, when the maximum lapse time is closer to the S-wave traveltime, the single scattering phenomena prevail in the coda composition, and Q_c is closer to Q_t; at longer time intervals the coda waves begin to be enriched by multiply scattered waves, and in this case Q_c approaches Q_i (Mayor *et al.* 2016). In synthesis, in the range of the coda time intervals above indicated, for increasing l_0 Q_c tends to Q_i, while in earth media characterized by strong heterogeneity (short l_0), Q_c depends also on the degree of heterogeneity, and is closer to Q_t than to Q_i (Del Pezzo & Ibáñez 2020). From the above discussion it emerges that Q_c cannot be seen as a rock attribute as its relation with the elastic property of the rocks is unclear, rather it is a coefficient describing the energy propagation.

The reason why Q_c, and not the couple Q_i and Q_s , is still used to characterize the space distribution of the seismic attenuation, is that in the fit of the observed seismogram energy envelope, there is a strong trade-off between Q_i and Q_s.

3.2 The weighting functions for *Q*-coda imaging

The first Q-coda image (2-D) was obtained by Singh & Herrmann (1983). These authors assigned the single Q_c values to the middle point of the segment connecting source and receiver, and then composed the image using spatial smoothing. Xie & Mitchell (1990) described a back-projection procedure, based on assigning the measured Q_c values to any point (with the same probability) in the whole scattering ellipse, which was used as a very simplified weighting function. More recently, Calvet *et al.* (2013) and De Siena *et al.* (2016) jointly used Q_c and the S-wave envelope peak delay (proportional to Q_s) as observables to draw a 2-D picture of attenuation respectively in Pyrhenees and Saint Helens volcano. In the imaging procedure Calvet *et al.* (2013) still use a very simplified weighting function for Q-coda, similar to that described by Xie & Mitchell (1990), while De Siena *et al.* (2016) use a weighting function similar to that in this paper.

In this paper, we use the approach described by Del Pezzo *et al.* (2018) to calculate a polynomial approximation of the sensitivity kernel for Q-coda discussed by Pacheco & Snieder (2006), which we use in the present approach as weighting functions, heuristically giving them a probabilistic meaning. Detailed studies on sensitivity kernels for the scattering can be found in Pacheco & Snieder (2005), Obermann *et al.* (2013) Planès *et al.* (2014), Mayor *et al.* (2014), Margerin *et al.* (2016) and Zhang *et al.* (2021). The polynomial approximation of the sensitivity kernel for Q-coda is given by the equation described in Appendix A. In Fig. 2 we show a contour plot example of its space pattern.

3.3 The method of imaging

The method used in this paper to construct the images is described in detail in Del Pezzo & Ibáñez (2020). Here only a brief outline will be given. The method consists in estimating $\overline{q_i}$, the estimate of Q_c for the ith source–receiver couple, where i spans over all the N couples. The volume under study is divided in cells. $\overline{q_i}$ is then assigned to the jth space cell, weighted by the weighting function correspondent to the the ith couple, $w(x_j, y_j, z_j, r_i, t_l, v)$, here denoted as w_{ij}. w_{ij} represents the probability that, for the ith source–receiver couple positioned respectively at $\{x_{si}, y_{si}, z_{si}\}$ and $\{x_{ri}, y_{ri}\}$, the product $\overline{q_i} w(x_j, y_j, z_j, r_i, t_l, v)$ (see Appendix A for the analytic expression of the function w) is calculated for any couple (index i) and in the center of any cell (index j), and will be indicated for simplicity $\overline{q_i} w_{ij}$. r_i indicates the distance between the source and receiver and t_l the maximum lapse time.

The best estimator of Q_c in the jth cell, Q_{cj} , will be given by

$$Q_{cj} = \frac{\sum_i \overline{q_i} w_{ij}}{\sum_i w_{ij}}. \tag{3}$$

3.4 Data analysis

For this work we used 1600 earthquakes with magnitudes placed in the interval $2.0 < M_L < 4.5$ located in Mt. Etna edifice for the time interval of 2006–2019 and recorded by the permanent seismic network of the Istituto Nazionale di Geofisica e Vulcanologia-Osservatorio Etneo (INGV-OE). All the seismic stations used for the present analysis were equipped with three-component, broadband (0.01–40 s period), 24-bit resolution seismometers, digitizing the signals at 100 samples per second. The data set including P- and S-wave arrival times, location parameters and raw seismic waveforms,

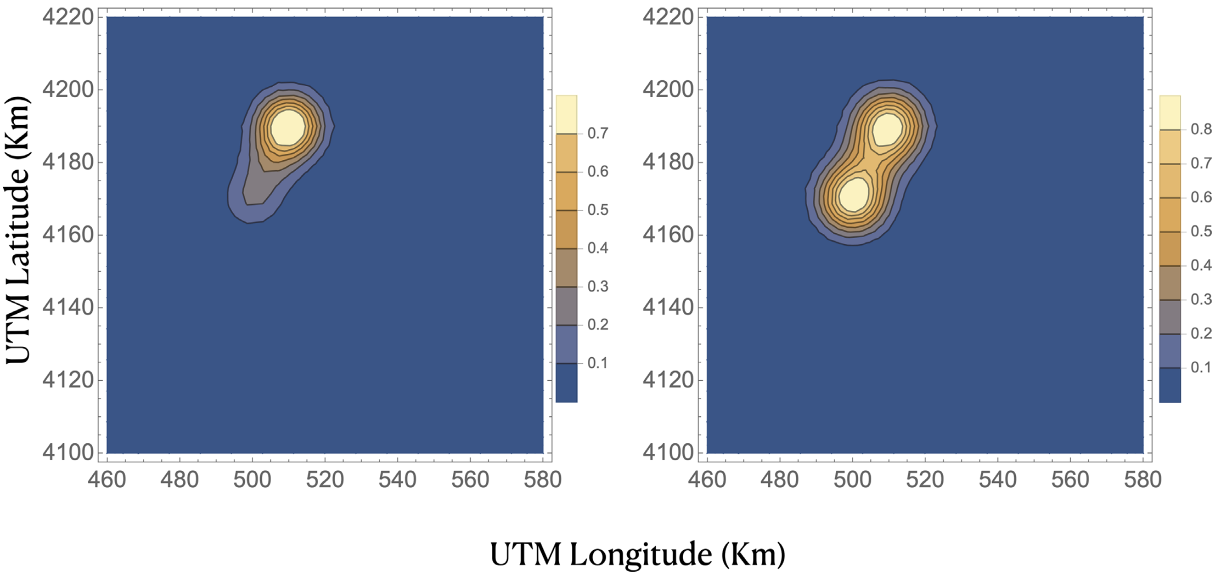

Figure 2. Left-hand panel: Isolines of function w calculated fixing the depth at 0.1 km for a source located at UTM Longitude 500.0, UTM latitude 4170.0, depth 10.0 km, and a receiver at UTM longitude 510.0, UTM latitude 4190.0, located at surface. Right-hand panel: Isolines for a source located at the same epicentre as in the left-hand panel, at a depth of 0.0 km, with receiver in the same position.

were downloaded from the INGV-OE data base and catalogue (Alparone *et al.* 2015) and (Alparone *et al.* 2020).

The selection of the data set was done on the base of the best located earthquakes, fulfilling the constraints of having at least 6 *P*- and 2 *S*-arrival times, a root mean squared traveltime residual, RMS, lower than 1s, azimuthal gap smaller than 180° and hypocentral errors smaller than 1.0 km. A final set of 5695 three component seismograms was used for the coda-*Q* analysis.

$\overline{q_i}$, the estimate of Q_c for the ith source receiver couple, was estimated using the following procedure. First, we estimated the energy envelope of the seismogram for the two horizontal components selecting for the analysis the signal starting at twice the *S*-wave traveltime and ending at 30 s from the origin time. We calculated the energy spectra of 3 s long time windows, sliding along the seismogram 1.5 s each step. For each spectrum the energy averaged in four successive frequency bands, centred, respectively, at f_c =1.5, 3.0, 6.0 and 12.0 Hz with a bandwidth in the interval between $f_c/2$ and $2f_c$ was estimated. The value of this average for each spectrum was attributed to the center of the time interval, finally obtaining the energy-time envelope. This approach is parallel to the ordinary method used first by Aki & Chouet (1975) where envelopes were estimated by filtering in separate frequency bands (see e.g. Giampiccolo & Tuvè 2018). The Parseval theorem ensures that in wide hypotheses, RMS of the filtered trace is equivalent to the integral of Fourier spectrum in the same frequency band used for filtering.

The envelopes then were log-averaged over the two horizontal components, and the quantity $\omega t/Q_c$ was estimated fitting the log-averaged envelope to eq. (2). $\overline{q_i}$ values were eventually calculated together with their uncertainty. $\overline{q_i}$ values with an uncertainty higher than 100 per cent of their value, were rejected. The vertical component was excluded due to its lower signal-to-noise ratio at the end of the coda, in comparison with the horizontal components. However, it was tested that this exclusion does not significantly change the *Q*-coda estimates. Fig. 3 shows an example seismogram (three components) together with the spectra of the first time window, starting at twice the *S*-wave traveltime and the last one in the late coda, starting at 27 s after the origin time.

3.5 Results

The average of $\overline{q_i}$ (over the N source–receiver couples), $< \overline{q}_i >_N$, is reported in Table 1.

In the same table we provide the averages $< \overline{q}_i >_N$ estimated for two focal depth ranges: (i) ranging between surface and 18 km (crustal earthquakes); (ii) ranging from 18 to 35 km (upper mantle earthquakes). It is remarkable that $< \overline{q}_i >_N$ for crustal and upper mantle earthquakes are coincident inside the uncertainties at all frequencies.

According to this observation we can assume that the attenuation effects in the upper part of lithosphere beneath Mt Etna show no variation with depth. This assumption is complemented by a previous attenuation study (Ibáñez *et al.* 2020) in the same area, carried out with the objective to separately obtain the contribution of intrinsic and scattering attenuation parameters in the upper part of the crust. Ibáñez *et al.* (2020), using active data, measured Q_i and Q_s in the shallowest part of the crust, showing that Q_i spans from 34 in the frequency band centered at 4 Hz, to 200 at 20 Hz, while Q_s spans respectively from 10 to 50. These values indicate that in the first 2–3 km below the surface scattering phenomena prevail on the intrinsic dissipation, for the whole frequency band analyzed.

Using a passive data set in a depth range compared to that of this study with a number of events smaller than the present one, Del Pezzo *et al.* (2015, 2019) show that space averaged scattering attenuation prevails over intrinsic attenuation at low frequency, while Q_i and Q_s are comparable at higher frequency. Comparing the results reported in these last two papers with the Q_c values estimated in this paper, it results that Q_c is very close to Q_s at 1.5 Hz; is comparable with Q_t between 3 and 6 Hz and approaches Q_i at high frequency (12 Hz). Preliminary results from a new attenuation study, which will submitted soon for publication (Giampiccolo *et al.*, in preparation), based on a revised MLTWA method applied to the present data set, confirms these previous results.

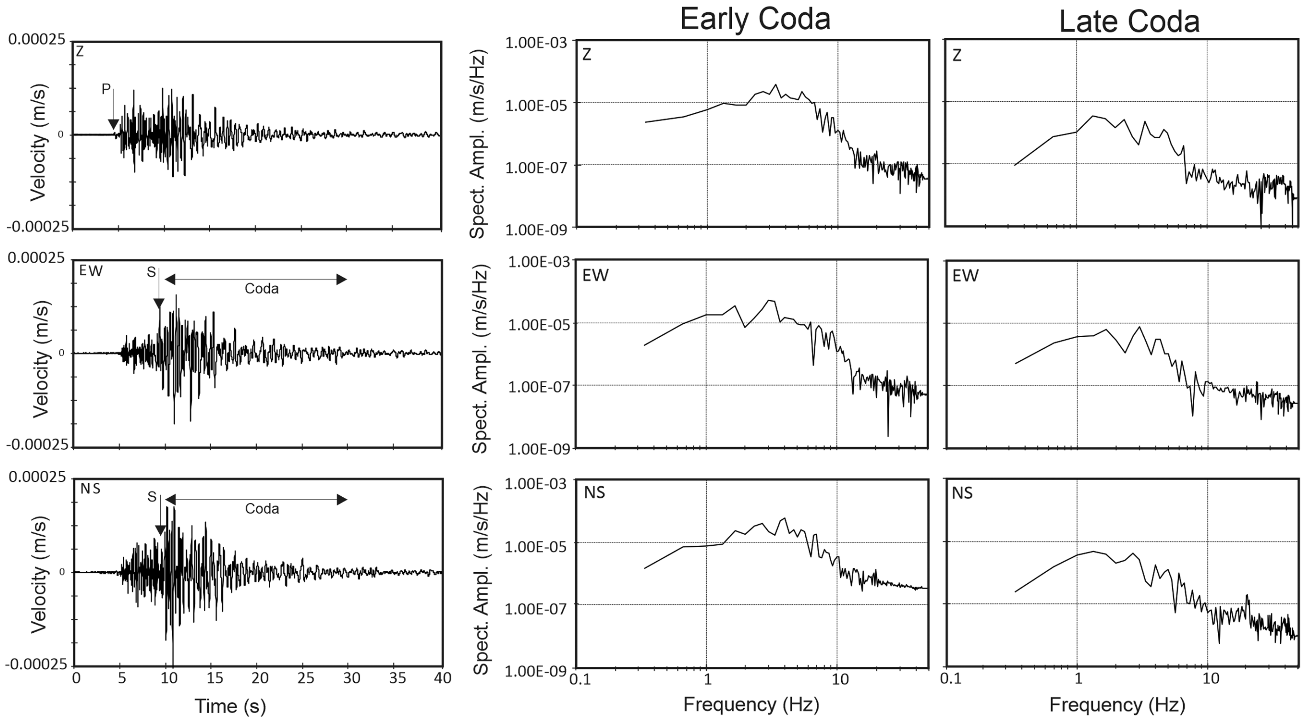

Figure 3. An example of seismograms (leftmost panels) for a shallow (h = 4 km) M_L = 3.4 earthquake recorded at ECTS station (epicentral distance = 25 km). From top to bottom Vertical (Z), east–west (EW), north–south (NS) components are shown. On the right-most panels, the amplitude spectra calculated in the early and late coda windows, respectively, for all components.

Table 1. Q-coda averaged over the source–receiver couples for the four frequency bands utilized.

	All depths ($N = 5935$)	
Frequency (Hz)	$< \overline{q}_i >_N$	σ_q
1.5	55.0	0.3
3.0	80.4	0.3
6.0	112.1	0.4
12.0	213.4	0.4
	Crustal earthquakes ($N = 4815$)	
Frequency (Hz)	$< \overline{q}_i >_N$	σ_q
1.5	54.1	0.4
3.0	79.9	0.4
6.0	111.7	0.4
12.0	216.9	0.4
	Mantle earthquakes ($N = 1120$)	
Frequency (Hz)	$< \overline{q}_i >_N$	σ_q
1.5	55.6	0.8
3.0	82.4	0.8
6.0	114.1	0.8
12.0	198.5	0.8

The images showing the space distribution of Q_c were obtained using the method described in Subsection 3.3. We considered the planes at 0, 5, 10, 15, 20, 25, 30 and 35 km, normal to the depth axis. Each plane was divided in squares with side of 5 km, and in the middle of the jth square we calculated $\overline{q_j}$ using eq. (3). The complete images shown in Figs 4 and 5 were eventually obtained using the graphical interpolation routines of *Mathematica*™. North–south and east–west vertical sections are reported in Fig. 6, showing the Q_c depth variation.

The uncertainties associated with Q_{cj} (pixel) values are estimated using eq. (B2) in Appendix B. The isolines of equal σ (standard deviation) for the frequency of 3 Hz are shown in Fig. 7 as an example. The uncertainties associated with the single-path estimates of Q_c span from about 10 to 35 (see their distribution in Fig. 8).

Uncertainties on Q_{cj} fall in the interval between 0.1 and 5. We thus decided to draw isolines spaced of 10 units in the images of Figs 4–6. In these images the color scale represents Q_{cj} values that are statistically different with high confidence level. The volume under study, which spans the whole Etna area, roughly corresponds to the zones with resolution (see eq. B3) greater than 0.1; this value is associated with maximum uncertainties of the order of 5 on Q_{cj} .

4 DISCUSSION

Differently from non-volcanic areas (see e.g. Akinci *et al.* 2020), Q_c averaged over the events in the Mt Etna area indicate high attenuation for any frequency band, as expected for an highly heterogeneous and complex volcanic region (Table 1). Moreover, the same Table shows that Q_c in the shallowest part of the crust and in the lower crust/upper mantle are practically coincident, indicating that attenuation does not decrease with depth in the first 35 km beneath Etna. While several studies (see e.g. Ibáñez *et al.* 1990) show that in general Q grows with depth, in our analysis, differently, we observe an almost uniform pattern, and in some areas even a decrease of Q-coda (increase of the attenuation) with depth. Consequently, at Mt Etna volcano the effect of the upper crust and lateral heterogeneity should be stronger than any depth dependence, contrarily to what is observed in other regions.

The average Q_c values (Table 1) and the images of Figs 4 and 5, and 6, show that (a) Q_c changes with the frequency bands investigated and (b) the space attenuation anomalies change their intensity with increasing frequency. The interpretation of the dependence of Q_c on frequency is open to discussion, as the physical meaning of Q_c itself is controversial, as commented in Section 3.1.

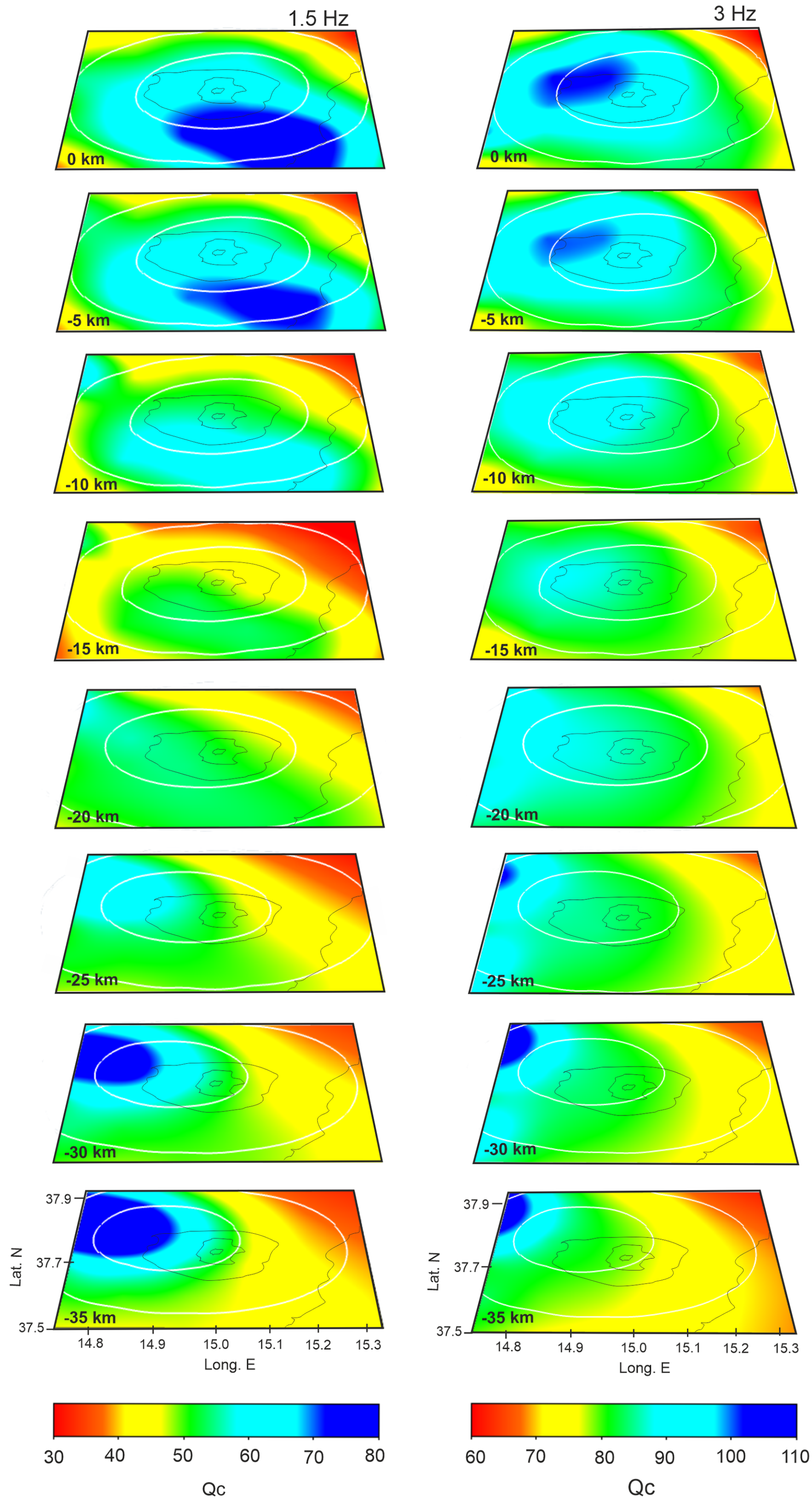

Figure 4. Slices of the 3-D Q-coda image cut from 0 to 35 km depth for the first 2 frequency bands analysed (1.5 and 3 Hz).

First, Q_c has an unclear physical meaning; second, it is an estimate of a combination of intrinsic- and scattering-Q which depends on the scattering regime in the zone of analysis; third, the model used to fit the observed energy envelopes assumes point-like scatterers, and uniform scattering. The frequency dependence may reasonably depend on the ratio between the wavelength and the average scatterer size, indicating how much the experimental reality differs from the model assumptions. In this paper we

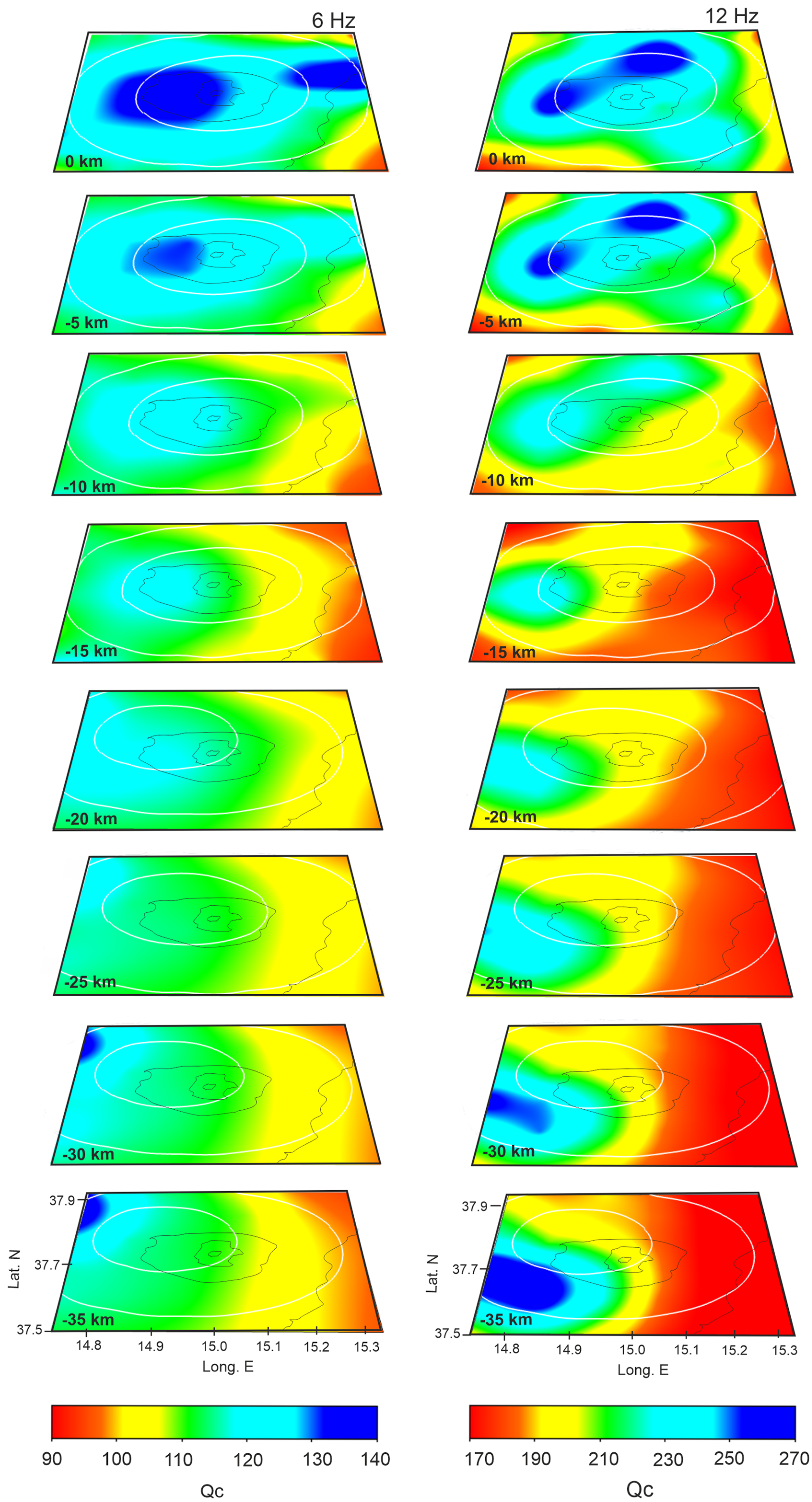

Figure 5. Slices of the 3-D *Q*-coda image cut from 0 to 35 km depth for the last 2 frequency bands analysed (6 and 12Hz).

assume that the waves with high wavelength (<6 Hz) could be affected by discontinuities and heterogeneities at large scale, while the coda waves in the 12 Hz band better reflect the smaller scale structures.

In the following we first briefly identify and discuss the presence of areas characterized by in depth and/or lateral attenuation contrasts. After that, we make an interpretation in the framework of the seismological, geological and volcanological evidences to-

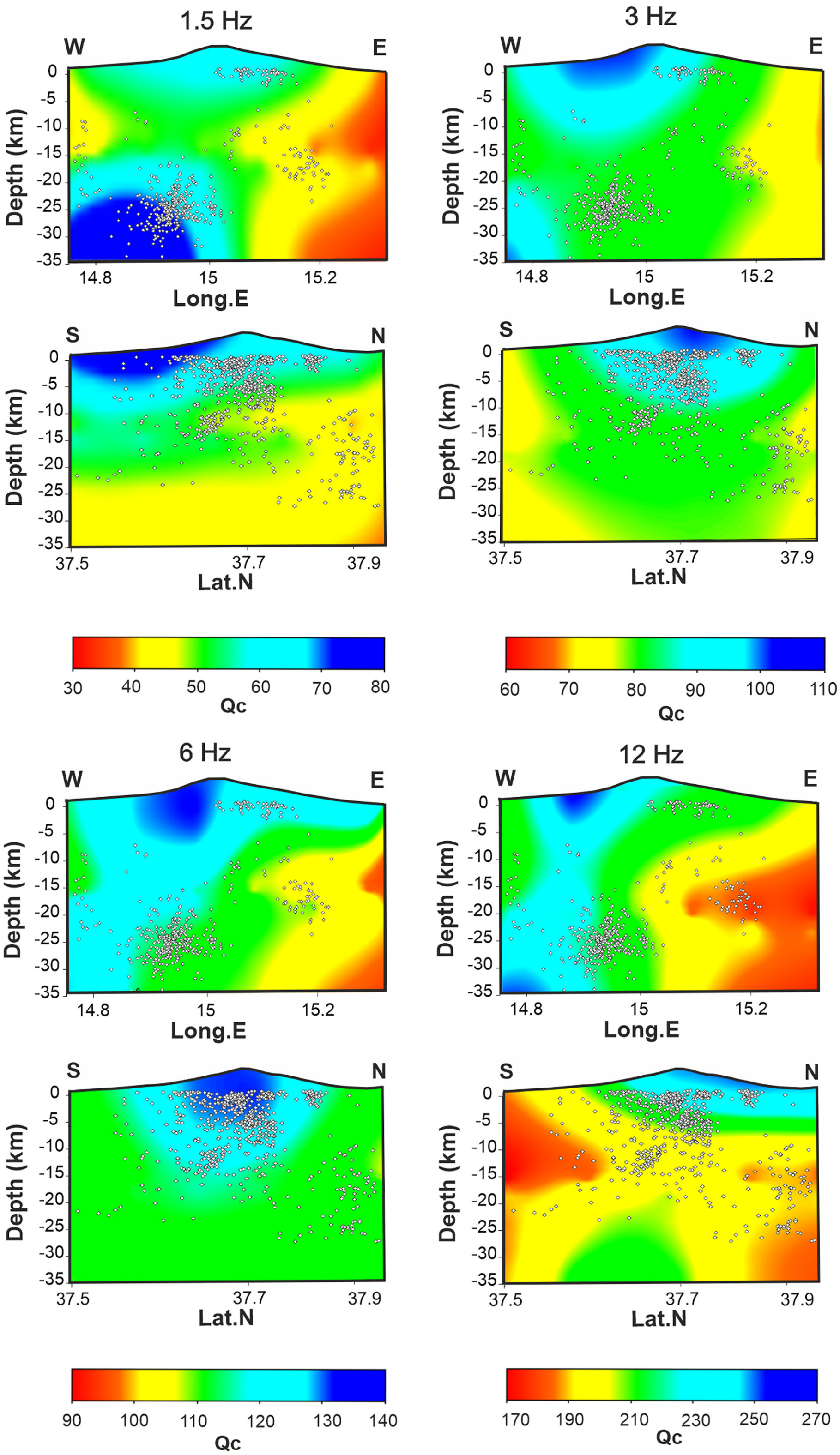

Figure 6. North–south and east–west vertical sections correspondent to the black dotted lines reported in Fig. 1, for the frequency bands centered at 1.5, 3.0, 6 and 12 Hz. Superimposed are the main topographical features and the earthquake sources. The color scale represents Q_c.

gether with the other velocity and attenuation images already available in the area. The first evidence is that the observed anomalies of Q_c can be associated with areas dominated by high structural complexities and are distributed along well-known tectonic structures which characterize the upper crust in the region of Etna volcano.

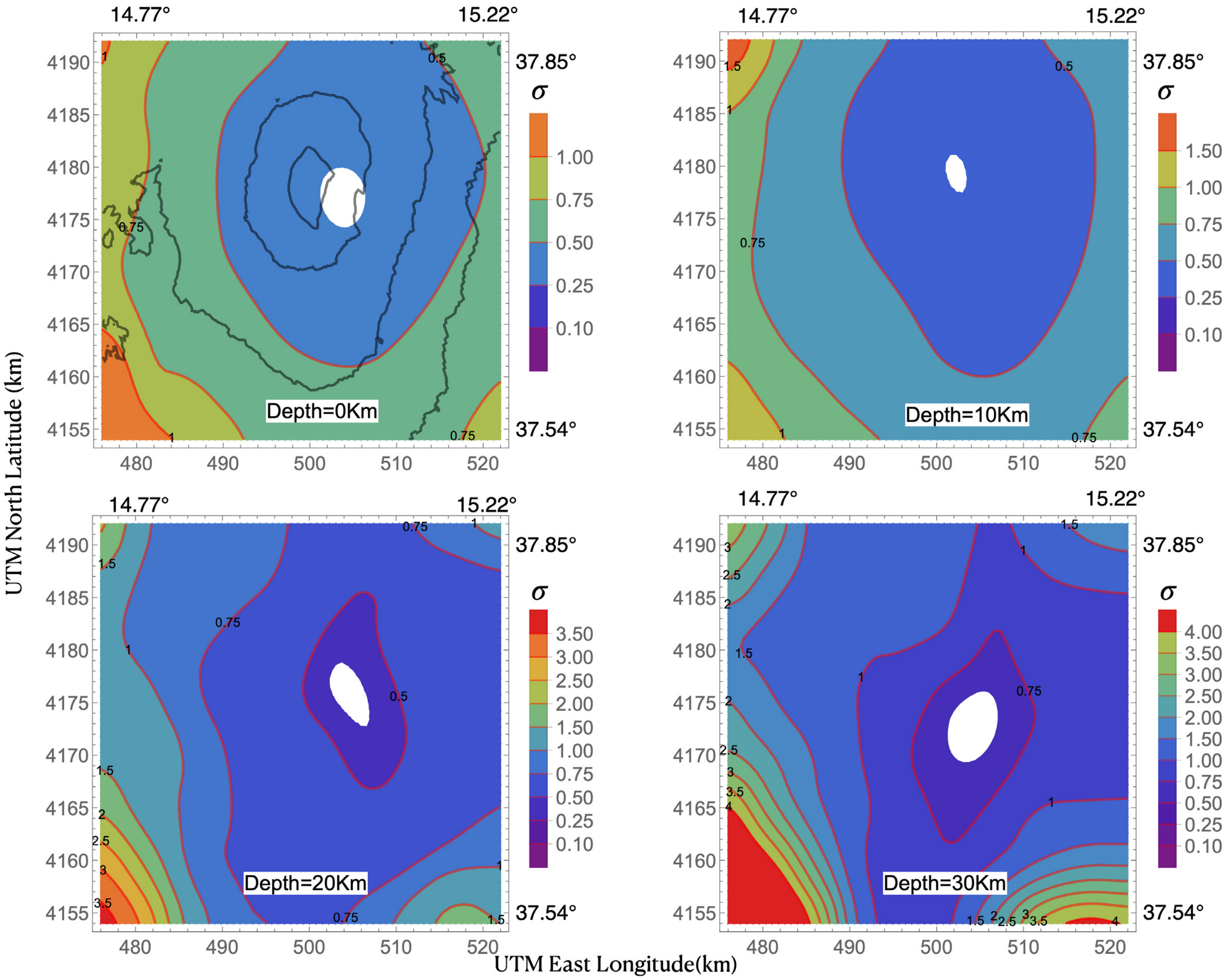

Figure 7. Horizontal slices of the space distribution of σ, the standard deviation calculated for the frequency of 3 Hz. Slices were drawn at the depths of 0, 10, 20 and 30 km.

As discussed above (Section 3.5), we assume that Q_c at low frequency (1.5 Hz) is close to Q_s. Consequently, the attenuation is almost entirely produced by strongly heterogeneous structures, like faults or fractures, which pump back the seismic energy to the receiver by reflection or refraction. The comparison with the 2-D image of separate Q_i and Q_s shown in Ibáñez *et al.* (2020) may be difficult, as the 2-D separate Q_i and Q_s images represent the attenuation in a shallow and thin (2 km thick) layer where most of the attenuation phenomena are governed by scattering. The present image at the shallowest depth, on the contrary, represent the first 5 km of crust below the surface, marked by a smaller average heterogeneity.

In detail, the Q_c contrasts observed at 1.5 Hz (Figs 4 and 6) are consistent with the direction of the most visible structural system present in the eastern flank of Mt Etna volcano (Fig. 1). Here, seismogenic faults NNW–SSE oriented along which the shallow seismicity ($h \leq 10$ km) is concentrated (Timpe Faults System, TFS; Fig. 1), represent the northernmost elongation of the Malta Escarpment, the main lithospheric structure in eastern Sicily (Bousquet & Lanzafame 2004). The Q_c contrasts delimit a wide volume marked by medium to high Q_c, elongated in the NW–SE direction, mostly extending from the southern flank of the volcanic edifice towards southeast. It is worth stressing that this high Q_c anomaly spatially correlates with the location of a high-velocity body, named in several works as HVB, and placed by many authors in the central-southern sector of Mt Etna and extending toward the eastern area, as evidenced in literature (e.g. Patanè *et al.* 2002, 2006; Barberi *et al.* 2004; De Gori *et al.* 2005, 2011b; Martinez-Arevalo *et al.* 2005; Alparone *et al.* 2012). This huge HVB has been recently well resolved by a recent velocity tomography (Vp and the ratio Vp/Vs) study, showing a refined structure from the surface up to a depth of 18 km (Giampiccolo *et al.* 2020), representing a massive accumulation of non-erupted volcanic material, emplaced during the recent and past volcanic activity in the sedimentary basement (Corsaro *et al.* 2004). Is very interesting to observe another high-velocity/high-Q anomaly placed in the southeast region of Mt Etna, previously highlighted by Dìaz-Moreno *et al.* (2018) and by Ibáñez *et al.* (2020) too. This last region can be correlated with a magnetic positive anomaly, considered as large and intense (>700 nT), that Cavallaro *et al.* (2016) associated with deep magmatic sources. Corsaro *et al.* (2004) explained that these magmatic bodies could be compatible with the existence of a feeding system of an ancient shield volcano located offshore of the Timpe area. At 3 and 6 Hz Q_c tends to be similar to Q_t, as observed by Del Pezzo *et al.* (2019). In general, higher Q_c

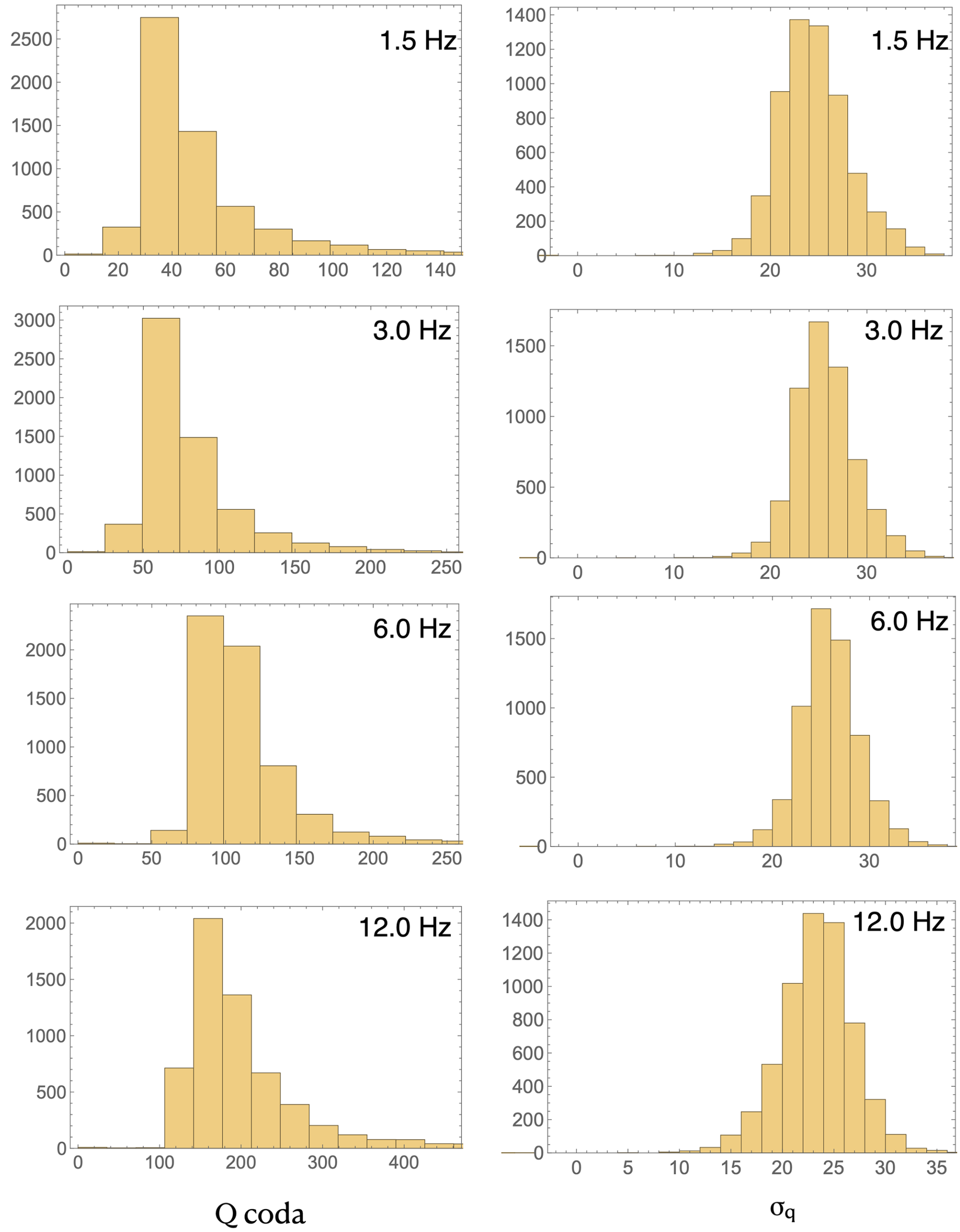

Figure 8. Histogram of the single path Q_c estimates together with the histogram of their associated single path standard deviations.

values predominate in the western part of the volcano more than in the eastern flank. This finding is consistent with the structural setting of the western part of Mt Etna which is considered as the most stable. A major high Q_c zone, oriented NE–SW is clearly visible down to the depth of 5 km and vanishes at greater depths. Its southern edge is oriented along the direction of the Rift W (Fig. 1) which constitutes a structural limit between a very unstable flank, placed on the Southwest, and the observed steady zone toward the northwest. A minor high Q_c anomaly, visible only at 6 Hz in the same depth range, is observed ENE of the volcanic edifice. The location of this low attenuation volume, E–W oriented, is coincident with the position of the eastern segment of the PF (Fig. 1). This structure has an important role in controlling the dynamic of the eastern sector and represents the intersection between an unstable and a stable area (Alparone *et al.* 2013). At high frequency (12 Hz) intrinsic dissipation predominates over the scattering; consequently, the attenuation measured by Q_c is mainly attributable to an absorption effect. The images at high (12 Hz) frequency (Figs 5 and 6) show the strongest attenuation contrasts at all depths, with Q_c changes up to 30 per cent with respect to the average. The first feature is a high Q_c anomaly located in the western sector of the volcano, approximately in the same position of the anomaly observed at 3 and 6 Hz. A second high Q_c anomaly is located to the NE of the summit craters. This anomaly correlates with a high *P*-wave velocity volume observed by Giampiccolo *et al.* (2020), close to the central-western sector of PF (Fig. 1). The western limit of this anomaly marks the boundary with a highly fractured zone corresponding to the NE Rift (Fig. 1), one of the zones where is placed a main magma intrusion below the volcano. On the eastern side, a low Q_c lobe extends from the crater area towards southeast, and coincides with the zone where most of the shallow fractures are located. In overall, at all frequencies, low Q_c mostly characterize the whole investigated area up to the depth of 20 km. It is worth stressing that low *Vp* and high *Vp*/*Vs* have been observed all around the volcanic edifice, up to 18 km b.s.l. by Giampiccolo *et al.* (2020). As also reported by these authors, the association of low *Vp* with low Q_p and high *Vp*/*Vs* testifies the possible presence around Mt Etna of large volumes of overpressurized fluids within the sedimentary units. In many of these zones it is observed a large rate of seismicity that can be the consequence of micro-cracking generated by the high pore-pressure (Giampiccolo *et al.* 2020). Some high Q_c volumes are observed to the west of the volcanic edifice. At 1.5 and 12 Hz these volumes correlate well with the distribution of the deep seismicity (20–35 km), which characterizes the western sector of the volcano. This sector, according to literature, is linked with the regional tectonic processes associated with the compressive regime at the front of the Apennine Maghrebian Chain (Catalano *et al.* 2004; Lavecchia *et al.* 2007; Sicali *et al.* 2014; De Guidi *et al.* 2014; Scarfì *et al.* 2016). The deep seismicity has been indicated by Lavecchia *et al.* (2007) as originated from segments of the so called 'Sicilian Basal Thrust', a regional scale deep crustal structure. The existence of this geological structure was confirmed on the base of earthquake focal mechanisms, geodetic data and field studies, which indicated the evidence of active folds and thrust deformation zones located South of the volcanic edifice (De Guidi *et al.* 2014).

5 CONCLUSIONS

3-D direct *P*-wave or *S*-wave attenuation (total-*Q*, Q_t) tomography is confirmed as one of the most useful tools to image geological structures in general; in particular, for volcano structures, this procedure is very interesting since permits to associate physical parameters related to the decrease of transmitted energy with the feeding conduits and magma chambers, contributing to the modeling of volcano dynamics. Despite this positive prospective, attenuation tomographies carried out so far at volcanoes are mainly based on the measurement of the sole *P*-wave attenuation. On the other hand, information derived from the *S*-waves attenuation is extremely useful in the interpretation of the volcanic dynamic and rock properties as *S*-waves attenuation anomalies are directly associated with the thermally weakened crust in volcanoes much more than *P* wave ones.

As we have evidenced in this work, the diffusive (scattering) wave field can entirely fill this lack, since coda waves are predominantly composed by *S* waves, and they are much more easily analysable than the direct *S* waves. This is the reason why the study of the space distribution of Q_c values is now starting to be used to improve the reconstructions of the tectonic and geological features at a crustal-scale, providing additional information about the fluid content. In this study, for the first time we employ a 3-D approach based on the *Q*-coda attenuation kernels to map shallow crust and upper mantle in the Mt Etna area at different frequencies. This approach provides a marked improvement in the geological interpretation, if compared with the information given by the measure of Q_c averaged over the area.

In fact, since it is based on the analysis of (single or multiple) scattered waves sampling large volumes of the volcanic structure, the obtained results add details in the medium characteristics at the roots of Mt Etna and helps to understand the tectonic complexity of the crust and upper mantle of this region. In the upper crust, regions of highest structural complexities are associated with evident Q_c anomalies and they are distributed along well known tectonic structures in the crust of Mt Etna area. In every frequency band, low Q_c values (as compared with a world average) mostly characterize the whole region, in agreement with low *Vp* and high *Vp*/*Vs* observed all around the volcanic edifice, down to 18 km b.s.l., by Giampiccolo *et al.* (2020). Following these authors our results confirm the existence of a very large hydrothermal system associated with the sedimentary units placed around the volcanic edifice that contain wide volumes overpressured by fluids. In the middle crust/upper mantle transition zone, below 20 km of depth, the present images show a structure more homogeneous than that at shallower depth. High Q_c volumes, observed to the west of the volcanic edifice, are correlated with the regional tectonic dynamics. The present results add information about the lower crust/upper mantle, between the depths of 20 and 35 km, where previous information was only marginal. However, as Q_c is a complex combination of the inelastic and scattering attenuation, the interpretation is still incomplete. A separate (Q_i and Q_s) 3-D attenuation image is still quite hard to obtain, due to the intrinsic difficulties in estimating separate observables in a single seismogram. This achievement will be our challenge for future studies.

ACKNOWLEDGEMENTS

The comments from an anonymous reviewer, from Chandrani Singh and from the Associate Editor greatly improved the quality of the manuscript. This work was partially funded by the Spanish Ministry of Economy and Competitiveness (MINECO) Project FEMALE, PID2019-106260GB-I00 and Progetto Ministry of Instruction, University and Research of Italy (MIUR) 2020-2029 Pianeta Dinamico (INGV 2021). Author contributions: E. Del Pezzo, E. Giampiccolo and T. Tuvé analyzed the results and prepared the figures; T. Tuvé and E. Giampiccolo prepared the data base; G. Di Grazia supervised the Geological part; J.M. Ibañez, E. Del Pezzo and E. Giampiccolo supervised the text draft.

DATA AVAILABILITY

The data underlying this paper consist of the seismograms recorded by INGV seismic network operating for the monitoring of Etna Volcano and will be shared on reasonable request to the first author.

REFERENCES

Aki, K. & Chouet, B., 1975. Origin of coda waves: Source, attenuation, and scattering effects, *J. geophys. Res.,* **80**(23), 3322–3342.

Akinci, A., Del Pezzo, E. & Malagnini, L., 2020. Intrinsic and scattering seismic wave attenuation in the Central Apennines (Italy), *Phys. Earth planet. Inter.,* **303,** 106498.

Aloisi, M., Cocina, O., Neri, G., Orecchio, B. & Privitera, E., 2002. Seismic tomography of the crust underneath the Etna volcano, Sicily, *Phys. Earth planet. Inter.,* **134,** 139–155.

Alparone, S., Barberi, G., Cocina, O., Giampiccolo, E., Musumeci, C. & Patanè, D., 2012. Intrusive mechanism of the 2008–2009 Mt. Etna eruption: Constraints by tomographic images and stress tensor analysis., *J. Volc. Geother. Res.,* **229-230,** 50–63.

Alparone, S., Cocina, O., Gambino, S., Mostaccio, A., Spampinato, S., Tuvè, T. & Ursino, A., 2013. Seismological features of the Pernicana-Provenzana Fault System (Mt. Etna, Italy) and implications for the dynamics of northeastern flank of the volcano, *J. Volc. Geotherm. Res.,* **118,** 1–11.

Alparone, S. *et al.*, 2015. Instrumental seismic catalogue of Mt. Etna earthquakes (Sicily, Italy): ten years (2000-2010) of instrumental recordings, *Ann. Geophys,* **58**(4), S0435.

Alparone, S.C. *et al.*, 2020. Mt. Etna Revised and Concise Seismic Catalog from 1999 (EtnaRCSC) [Data set]. Istituto Nazionale di Geofisica e Vulcanologia (INGV).

Azzaro, R., Branca, S., Gwinner, K. & Coltelli, M., 2012. The volcano-tectonic map of Etna volcano, 1:100.000 scale: an integrated approach based on a morphotectonic analysis from high-resolution DEM constrained by geologic, active faulting and seismotectonic data, *Ital. J. Geosci.,* **131**(1), 153–170.

Azzaro, R., D'Amico, S., Peruzza, L. & Tuvè, T., 2013. Probabilistic seismic hazard at Mt. Etna (Italy): the contribution of local fault activity in mid-term assessment, *J Volcanol. Geotherm. Res.,* **251,** 158–169.

Azzaro, R., Barberi, G., D'Amico, S., Pace, B., Peruzza, L. & Tuvè, T., 2017. When probabilistic seismic hazard climbs volcanoes: the Mt. Etna case, Italy–Part 1: model components for sources parameterization., *Nat. Haz. Earth Syst. Sci.,* **17,** 1981–1998.

Barberi, G., Cosentino, M., Gervasi, A., Guerra, I., Neri, G. & Orecchio, B., 2004. Crustal seismic tomography in the Calabrian Arc region, South Italy, *Phys. Earth planet. Inter.,* **147**(4), 297–314.

Bonforte, A. & Puglisi, G., 2003. Magma uprising and flank dynamics on Mount Etna volcano, studied using GPS data (1994–1995)., *J. geophys. Res.,* **108**(2153), doi:10.1029/2002JB001845.

Borgia, A., Ferrari, L. & Pasquarè, G., 1992. Importance of gravitational spreading in the tectonic and volcanic evolution of Mount Etna., *Nature,* **357,** 231–235.

Bousquet, J. & Lanzafame, G., 2004. The tectonics and geodynamics of Mt. Etna: synthesis and interpretation of geological and geophysical data, in *Mt. Etna: Volcano Laboratory,* Vol. **143,** Geophysical Monograph Series, eds Bonaccorso, A., Calvari, S., Coltelli, M., Del Negro, C. & Falsaperla, S., AGU.

Branca, S. & Ferrara, V., 2013. The morphostructural setting of Mount Etna sedimentary basement (Italy): Implications for the geometry and volume of the volcano and its flank instability, *Tectonophysics,* **586,** 46–64.

Calvet, M., Sylvander, M., Margerin, L. & Villasenor, A., 2013. Spatial variations of seismic attenuation and heterogeneity in the Pyrenees: coda Q and peak delay time analysis, *Tectonophysics,* **608,** 428–439.

Cardaci, C., Coviello, M., Lombardo, G., Patanè, G. & Scarpa, R., 1993. Seismic tomography of Etna volcano, *J. Volc. Geotherm. Res.,* **56,** 357–368.

Cassinis, R., Finetti, I., Giese, P., Morelli, C., Steinmetz, L. & Vecchia, O., 1969. Deep seismic refraction research on Sicily, *Boll. Geof. Teor. Appl.,* **11,** 140–160.

Catalano, S., Torrisi, S. & Ferlito, C., 2004. The relationship between Late Quaternary deformation and volcanism of Mt. Etna (eastern Sicily): new evidence from the sedimentary substratum in the Catania region, *J. Volc. Geotherm. Res.,* **132,** 311–344.

Cavallaro, D. *et al.*, 2016. Acquisition procedures, processing methodologies and preliminary results of magnetic and ROV data collected during the TOMO-ETNA experiment, *Ann. Geophys.,* **59**(4), S0431.

Chiarabba, C., Amato, A., Boschi, E. & Barberi, F., 2000. Recent seismicity and tomographic modeling of the Mount Etna plumbing system, *J. geophys. Res.,* **105,** 10 923–10 938.

Chiarabba, C., De Gori, P. & Patanè, D., 2004. The Mt. Etna plumbing system: the contribution of seismic tomography, in *Mt. Etna: Volcano Laboratory,* Vol. **143,** Geophysical Monograph Series, AGU.

Clocchiatti, R., Condomines, M., Guenot, N. & Tanguy, J., 2004. Magma changes at Mount Etna: the 2001 and 2002–2003 eruptions., *Earth planet. Sci. Lett.,* **226,** 397–414.

Continisio, R., Ferrucci, F., Gaudiosi, G., Lo Bascio, D. & Ventura, G., 1997. Malta escarpment and Mt. Etna: early stages of an asymmetric rifting process? Evidences from geophysical and geological data., *Acta Vulcanol.,* **9,** 45–53.

Corsaro, R.A., Rotolo, S.G., Cocina, O. & Tumbarello, G., 2004. Cognate xenoliths in Mt. Etna lavas: witnesses of the high-velocity body beneath the volcano, *Bull. Volcanol*., **76**(816), 12.

De Gori, P., Chiarabba, C. & Patanè, D., 2005. Qp structure of Mount Etna: constraints for the physics of the plumbing system, *J. geophys. Res.,* **110**(B05303), doi:10.1029/2003JB002875.

De Gori, P., Chiarabba, C., Giampiccolo, E., Martinez-Arevalo, C. & Patanè, D., 2011a. Body wave attenuation heralds incoming eruptions at Mount Etna, *Geology,* **39**(5), 503–506.

De Gori, P., Chiarabba, C., Giampiccolo, E., Martinez-Arevalo, C. & Patanè, D., 2011b. Body wave attenuation heralds incoming eruptions at Mt. Etna, *Geology,* **39,** 503–506.

De Guidi, G., Imposa, S., Scudero, S. & Palano, M., 2014. New evidence for Late Quaternary deformation of the substratum of Mt. Etna volcano (Sicily, Italy): clues indicate active crustal doming, *Bull. Volcanol.,* **76,** doi:10.1007/s00445-014-0816-8.

De Siena, L., Del Pezzo, E., Thomas, C., Curtis, A. & Margerin, L., 2013. Seismic energy envelopes in volcanic media: in need of boundary conditions, *Geophys. J. Int.,* **195**(2), 1102–1119.

De Siena, L., Calvet, M., Watson, K.J., Jonkers, A.R.T. & Thomas, C., 2016. Seismic scattering and absorption mapping of debris flows, feeding paths, and tectonic units at Mount St. Helens volcano, *Earth planet. Sci. Lett.,* **442**(C), 21–31.

Del Pezzo, E., 2008. Seismic wave scattering in volcanoes, *Adv. Geophys.,* **50,** 353–371.

Del Pezzo, E. & Ibáñez, J.M., 2020. Seismic coda-waves imaging based on sensitivity kernels calculated using an heuristic approach., *Geosciences,* **10,** 304.

Del Pezzo, E., Bianco, F., Giampiccolo, E., Tusa, G. & Tuve, T., 2015. A reappraisal of seismic Q evaluated at Mt. Etna volcano. Receipt for the application to risk analysis, *J. Seismol.,* **19,** 105–119.

Del Pezzo, E., Ibañez, J.M., Prudencio, J., Bianco, F. & De Siena, L., 2016. Absorption and scattering 2-D volcano images from numerically calculated space-weighting functions, *Geophys. J. Int,* **206,** 742–756.

Del Pezzo, E., De La Torre, A., Bianco, F., Ibáñez, J.M., Gabrielli, S. & De Siena, L., 2018. Numerically calculated 3D space-weighting functions to image crustal volcanic structures using diffuse coda waves, *Geosciences,* **8**(5), 175–13.

Del Pezzo, E., Giampiccolo, E., Tuvè, T., Di Grazia, G., Gresta, S. & Ibáñez, J.M., 2019. Study of the regional pattern of intrinsic and scattering seismic attenuation in Eastern Sicily (Italy) from local earthquakes, *Geophys. J. Int.,* **218,** 1456–1468.

Dìaz-Moreno, A. *et al.*, 2018. New insights on Mt. Etna's Crust and relationship with the regional tectonic framework from joint active and passive P-wave seismic tomography, *Surv. Geophys.,* **39**(1), 57–97.

Eulenfeld, T. & Wegler, U., 2016. 2016. measurement of intrinsic and scattering attenuation of shear waves in two sedimentary basins and comparison to crystalline sites in germany, *Geophys. J. Int.,* **205,** 744–757.

Eulenfeld, T. & Wegler, U., 2017. Crustal intrinsic and scattering attenuation of high-frequency shear waves in the contiguous united states., *J. geophys. Res.,* **122**(6), 4676–4690.

Faccenna, C., Becker, T., Lucente, F., Jolivet, L. & Rossetti, F., 2001. History of subduction and back-arc extension in the central Mediterranean, *Geophys. J. Int.,* **145,** 809–820.

Federico, C., Longo, M., D'Alessandro, W., Bellomo, S., Bonfanti, P. & Brusca, L., 2017. Hydrological versus volcanic processes affecting fluid circulation at Mt. Etna: inferences from 10 years of observations at the volcanic aquifer, *Chem. Geol.,* **452,** 71–84.

Gaebler, P.J., Eulenfeld, T. & Wegler, U., 2015. Seismic scattering and absorption parameters in the w-bohemia/vogtland region from elastic and acoustic radiative transfer theory., *Geophys. J. Int.,* **203**(3), 1471–1481.

Giampiccolo, E. & Tuvè, T., 2018. Regionalization and dependence of coda Q on frequency and lapse time in the seismically active Peloritani region (Northeastern Sicily, Italy), *J. Seismol.,* **22**(4), 1059–1074.

Giampiccolo, E., Cocina, O., De Gori, P. & Chiarabba, C., 2020. Dyke intrusion and stress-induced collapse of volcano flanks: the example of the 2018 event at Mt. Etna (Sicily, Italy), *Nat. Res. - Scient. Rep.,* **10,** 6373.

Gvirtzman, Z. & Nur, A., 1999. The formation of Mount Etna as the consequence of slab rollback., *Nature,* **401,** 782–785.

Hirn, A., Nercessian, A., Sapin, M., Ferrucci, F. & Wittlinger, G., 1991. Seismic heterogeneity of Mt. Etna: structure and activity, *Geophys. J.Int.,* **105,** 139–153.

Hirn, A., Nicolich, R. & Gallart, J., 1997. Roots of Etna volcano in faults of great earthquakes., *Earth Planet. Sci. Lett.,,* **148,** 171–191.

Ibáñez, J.M., Del Pezzo, E., Herraiz, M., Alguacil, G. & Morales, J., 1990. Depth-dependent seismic attenuation in the Granada zone (Southern Spain), *Bull. seism. Soc. Am.,* **80**(5), 1232–1244.

Ibáñez, J.M., Castro-Melgar, I., Cocina, O., Zuccarello, L., Branca, S., Del Pezzo, E. & Prudencio, J., 2020. First 2-d intrinsic and scattering attenuation images of Mt Etna volcano and surrounding region from active seismic data, *Geophys. J. Int.,* **220**(1), 267–277.

Laigle, M., Hirn, A., Sapin, M., Lépine, J.-C., Diaz, J. & Gallart, J., 2000. Mount Etna dense array local earthquake P and S tomography and implications for volcanic plumbing, *J. geophys. Res.,* **105,,** 21 633–21 646.

Larose, E., Planès, T., Rossetto, V. & Margerin, L., 2010. Locating a small change in a multiple scattering environment, *Appl. Phys. Lett.,* **96**(20), 204101.

Lavecchia, G., Ferrarini, F., De Nardis, R., Visini, F. & Barbano, M.S., 2007. Active thrusting as a possible seismogenic source in Sicily (Southern Italy): some insights from integrated structural kinematic and seismological data, *Tectonophysics,* **445**(3–4), 145–167.

Lentini, F., 1982. The geology of the Etna basement, *Mem. Soc. Geol. Ital.,* **23,** 7–25.

Lo Giudice, E. &, Rasà, 1992. Very shallow earthquakes and brittle deformation in active volcanic areas: the Etnean region as example, *Tectonophysics,* **202,** 257–268.

Margerin, L., 2011. Seismic waves, scattering, in *Encyclopedia of Solid Earth Geophysics. Encyclopedia of Earth Sciences Series,* eds H.K., Gupta, pp. 1210–1223, Springer.

Margerin, L., Planès, T., Mayor, J. & Calvet, M., 2016. Sensitivity kernels for coda-wave interferometry and scattering tomography: theory and numerical evaluation in two-dimensional anisotropically scattering media, *Geophys. J. Int.,* **204,** 650–666.

Martinez-Arevalo, C., Patanè, D., Rietbrock, A. & Ibañez, J.M., 2005. The intrusive process leading to the Mt. Etna 2001 flank eruption: constraints from 3-D attenuation tomography, *Geophys. Res. Lett.,* **32**(21), L21309.

Mayeda, K., Koyanagi, S., Hoshiba, M., Aki, K. & Zeng, Y., 1992. A comparative study of scattering, intrinsic, and coda Q-1 for Hawaii, Long Valley, and central California between 1.5 and 15 Hz, *J. geophys. Res,* **97,** 6643–6659.

Mayor, J., Margerin, L. & Calvet, M., 2014. Sensitivity of coda waves to spatial variations of absorption and scattering: radiative transfer theory and 2-D examples, *Geophys. J. Int.,* **197**(2), 1117–1137.

Mayor, J., Calvet, M., Margerin, L., Vanderhaeghe, O. & Traversa, P., 2016. Crustal structure of the Alps as seen by attenuation tomography, *Earth planet. Sci. Lett.,* **439,** 71–80.

Mostaccio, A., Tuvè, T., Patanè, D., Barberi, G. & Zuccarello, L., 2013. Improving seismic surveillance at Mt. Etna volcano by probabilistic earthquake location in a 3D model, *Bull. seism. Soc. Am.,* **103**(4), 2447–2459.

Musumeci, C., Cocina, O., De Gori, P. & Patanè, D., 2004. Seismological evidence of stress induced by dike injection during the 2001 Mt. Etna eruption, *Geophys. Res. Lett.,* **31**(7),.

Obermann, A., Planès, T., Larose, E., Sens-Schönfelder, C. & Campillo, M., 2013. Depth sensitivity of seismic coda waves to velocity perturbations in an elastic heterogeneous medium, *Geophys. J. Int.,* **194**(1), 372–382.

Ogniben, L., 1966. Lineamenti idrogeologici dell' Etna, *Riv. Miner. Sicil.,* **100–102,** 24.

Paasschens, J., 1997. Solution of the time-dependent Boltzmann equation, *Phys. Rev. E,* **56**(1), 1135–1141.

Pacheco, C. & Snieder, R., 2005. Time-lapse traveltime change of multiply-scattered acoustic waves, *JASA,* **118**(3), 1300–1310.

Pacheco, C. & Snieder, R., 2006. Time-lapse traveltime change of singly scattered acoustic waves, *Geophys. J. Int.,* **165**(2), 485–500.

Patanè, D., Chiarabba, C., Cocina, O., De Gori, P., Moretti, M. & Boschi, E., 2002. Tomographic images and 3D earthquake locations of the seismic swarm preceding the 2001 Mt. Etna eruption: Evidence for a dyke intrusion, *Geophys. Res. Lett.,,* **29**(10), 135–1-135-4.

Patanè, D., Cocina, O., Falsaperla, S., Privitera, E. & Spampinato, S., 2004. Mt. Etna volcano: a seismological framework, in *Mt. Etna: Volcano Laboratory,* Vol. **143,** pp. 147–165, eds Calvari, S., Bonaccorso, A., Coltelli, M., Del Negro, C., & Falsaperla, S., AGU.

Patanè, D., Barberi, G., Cocina, O., De Gori, P. & Chiarabba, C., 2006. Time-resolved seismic tomography detects magma intrusions at Mount Etna, *Science,* **313,** 821–823.

Patanè, D., Aliotta, M., Cannata, A., Cassisi, C., Coltelli, M., Di Grazia, G., Montalto, P. & Zuccarello, L., 2011. Interplay between tectonics and Mount Etna's volcanism: insights into the geometry of the plumbing system, in *New Frontiers in Tectonic Research,* eds, Uri Shatner, IntechOpen.

Planès, T., Larose, E., Margerin, L., Rossetto, V. & Sens-Schönfelder, C., 2014. Decorrelation and phase-shift of coda waves induced by local changes: multiple scattering approach and numerical validation, *Waves Rand Complex Media,* **24**(2), 99–125.

Prudencio, J., De Siena, L., Ibanez, J.M., Del Pezzo, E., Garcia Yeguas, A. & Díaz-Moreno, A., 2015. The 3D attenuation structure of deception Island (Antarctica), *Surv. Geophys.,* **36**(3), 371–390.

Prudencio, J., Taira, T., Aoki, Y., Aoyama, H. & Onizawa, S., 2017. Intrinsic and scattering attenuation images of usu volcano, japan, *Bull. Volcanol.,* **79**(4), 29.

Prudencio, J., Del Pezzo, E., Garcia Yeguas, A. & Ibáñez, J.M., 2013a. Spatial distribution of intrinsic and scattering seismic attenuation in active volcanic islands - I: model and the case of Tenerife Island, *Geophys. J. Int.,* **195**(3), 1942–1956.

Prudencio, J., Ibáñez, J.M., Garcia Yeguas, A., Del Pezzo, E. & Posadas, A.M., 2013b. Spatial distribution of intrinsic and scattering seismic attenuation in active volcanic islands - II: Deception Island images, *Geophys. J. Int.,* **195**(3), 1957–1969.

Rittmann, A., 1973. Structure and evolution of Mount Etna, *Phil. Trans. R. Soc., Lond.,* **274A,** 5–16.

Rust, D. & Neri, M., 1996. The boundaries of large-scale collapse on the flanks of Mount Etna, Sicily., *Geol. Soc., Lond., Spec. Publ.,* **110,** 193–208.

Rust, D., Behncke, B., Neri, M. & Ciocanel, A., 2005. Nested zones of instability in the Mount Etna volcanic edifice, Sicily, *J. Volcanol. Geotherm. Res.,* **144,** 137–153.

Sato, H., 1977. Energy propagation including scattering effects. single isotropic scattering approximation, *J. Phys. Earth,* **25**(1), 27–41.

Sato, H., Fehler, M. & Maeda, T., 2012. *Seismic Wave Propagation and Scattering in the Heterogeneous Earth,* 2nd edn, Springer-Verlag.

Scarfì, L., Barberi, G., Musumeci, C. & Patanè, D., 2016. Seismotectonics of northeastern Sicily and southern Calabria (Italy): new constraints on the tectonic structures featuring in a crucial sector for the Central Mediterranean geodynamics., *Tectonics,* **34,** 812–832.

Sharp, A., Davis, P. & Gray, F., A low velocity zone beneath Mount Etna and magma storage 1980. *Nature,* **287,** 587–591.

Sicali, S., Barbano, M., D'Amico, S. & Azzaro, R., 2014. Characterization of seismicity at Mt. Etna volcano (Italy) by inter-event time distribution, *J. Volc. Geotherm. Res.,* **270,** 1–9.

Singh, S. & Herrmann, R.B., 1983. Regionalization of crustal coda Q in the continental United States, *J. geophys. Res.,* **88**(B1), 527–538.

Sketsiou, P., Napolitano, F., Zenonos, A. & De Siena, L., 2020. New insights into seismic absorption imaging, *Phys. Earth planet. Inter.,* **298,** doi:10.1016/j.pepi.2019.106337.

Snieder, R., 2006. The theory of coda wave interferometry, *Pure appl. Geophys.,***163,** 455–473.

Solaro, G., Acocella, V., Pepe, S., Ruch, J., Neri, M. & Sansosti, E., 2010. Anatomy of an unstable volcano from InSAR: multiple processes affecting flank instability at Mt. Etna, 1994–2008, *J. geophys. Res.,* **115,** B10405, doi:10.1029/2009JB000820.

Tanguy, J., Condomines, M. & Kieer, G., 1997. Evolution of Mount Etna magma: constraints on the present feeding system and eruptive mechanism, *J. Volc. Geotherm. Res.,* **75,** 221–250.

Urlaub, M., Petersen, F., Gross, F., Bonforte, A., Puglisi, G. & Guglielmino, F., 2018. Gravitational collapse of Mount Etna's southeastern flank, *Sci. Adv.,* **4**(10), doi:10.1126/sciadv.aat9700.

Xie, J. & Mitchell, B., 1990. A back-projection method for imaging large-scale lateral variations of Lg coda Q with application to continental Africa, *Geophys. J. Int.,* **100**(2), 161–181.

Zeng, Y., Su, F. & Aki, K., 1991. Scattering wave energy propagation in a random isotropic scattering medium. Part 1. Theory, *J. geophys. Res.,* **96,** 607–619.

Zhang, T., Sens-Schönfelder, C. & Margerin, L., 2021. Sensitivity kernels for static and dynamic tomography of scattering and absorbing media with elastic waves: a probabilistic approach, *Geophys. J. Int.,* **225**(3), 1824–1853.

APPENDIX A: THE APPROXIMATE 3D WEIGHTING FUNCTIONS

In the approach used in this paper, Q_{cj} is seen as a single measure of a repeated set of measures. The weighting functions in this approach give the probability that in the space point of given coordinates, the measure assumes effectively that value. The measure set thus produce for any pixel j, a set of point values of Q-coda multiplied by their probability, $\overline{q_i} w_{ij}$. We consider their weighted average as the characteristic value of Q-coda in the specific point. In other words, we simply 'project' the Q-coda measure, or 'attribute' the measure to a space point of given coordinates weighting for the weighting functions. A similar approach has been applied for example by Mayor *et al.* (2016), Prudencio *et al.* (2013a, 2017). The standard deviation of the Q-coda 'projected' into the 3-D volume under study can be easily calculated pixel by pixel, as an estimate of the uncertainty associated with the Q-coda pixel values . The 3-D weighting functions for Q-coda can be calculated as described in Del Pezzo & Ibáñez (2020) and in the references therein. Here we report its polynomial approximation used in the present approach, slightly modified from the one described in Del Pezzo & Ibáñez (2020) in the term which accounts for the distance dependence (eq. A4):

$$w(x, y, z, r, t_l, v) = \frac{f_1(x, y, z, r, t_l, v) + f_2(x, y, z, r, t_l, v)}{\mathrm{Max}(f_1 + f_2)}, \quad \text{(A1)}$$

where

$$f_1(x, y, z, r, t_l, v) = \frac{1}{2\pi\sigma(r, t_l, v)^3} \exp\left(-\frac{d_1^2}{2\sigma(r, t_l, v)^2}\right) + \frac{1}{2\pi\sigma(r, t_l, v)^3} \exp\left(-\frac{d_2^2}{2\sigma(r, t_l, v)^2}\right) \quad \text{(A2)}$$

$$f_2(x, y, z, r, t_l, v) = \frac{1}{6\pi\sigma(r, t_l, v)^3} \exp\left(-\frac{d_{1/2}^2}{2\sigma(r, t_l, v)^2}\right) \quad \text{(A3)}$$

$$\sigma(x, y, z, xs, ys, zs, xr, yr, t_l, v) = \frac{t_l v}{10} - \frac{r}{5} \quad \text{(A4)}$$

$$r = \sqrt{(xr - xs)^2 + (yr - ys)^2 + (-zs)^2}$$

$$d_1 = \sqrt{(x - xs)^2 + (y - ys)^2 + (z - zs)^2}$$

$$d_2 = \sqrt{(x - xr)^2 + (y - yr)^2 + z^2}$$

$$d_{1/2} = \sqrt{\left(x - \frac{xs + xr}{2}\right)^2 + \left(y - \frac{ys + yr}{2}\right)^2 + \left(z - \frac{zs}{2}\right)^2}$$

d_1 , d_2 and $d_{1/2}$ represent, respectively, the distance between the space coordinate and the source, between the space coordinate and the receiver and between the space coordinate and the source–receiver midpoint.

APPENDIX B: RESOLUTION AND UNCERTAINTIES

The Q-coda weighting functions (Del Pezzo & Ibáñez 2020) are here denoted as

$$w_{ij}(x_j, y_j, z_j, x_{ri}, y_{ri}, x_{si}, y_{si}, z_{si}),$$

w_{ij} represents the probability that, for the ith source–receiver couple positioned, respectively, at $\{x_{si}, y_{si}, z_{si}\}$ and $\{x_{ri}, y_{ri}\}$, the measured value of Q-coda effectively corresponds to the true value at the space point with coordinates x_j, y_j and z_j. For an exhausting review see Del Pezzo & Ibáñez (2020). j is the index associated with the jth pixel of generic coordinates $\{x, y\}$. i spans from 1 to N (N is the number of source–receiver couples in the data set). j spans from 1 to M where M is the number of cells in which the space has been divided (improperly called 'pixels'). $\overline{q_i}$ is the measure of Q_c for the ith source–receiver pair; $\overline{q}_j$ is the results for the jth pixel.

The 'back-projection' method yields

$$Q_{cj} = \frac{\sum_i \overline{q_i} w_{ij}}{\sum_i w_{ij}}. \quad \text{(B1)}$$

In this heuristic scheme, w_{ij} represents the unnormalized probability that the ith measure, $\overline{q_i}$, is associated with the jth pixel.

Calling σ_i the standard deviation correspondent to the ith measure, $\overline{q_i}$, and applying the ordinary error propagation equation to eq. (B1) we obtain

$$\sigma^2_{Q_{cj}} = \sum_i \left(\frac{\partial Q_{cj}}{\partial \overline{q_i}}\right)^2 \sigma_i^2 = \frac{1}{(\sum_i w_{ij})^2} \sum_i w_{ij}^2 \sigma_i^2. \quad \text{(B2)}$$

As can be immediately deduced, if $w_{ij} = 1$ and $\sigma_i = \sigma$ for every i and j , $\sigma_{q_j} = \frac{\sigma}{\sqrt{N}}$, as for the simple arithmetical average. We assume that the quantity proportional to the standard error inverse (normalized by σ), σ/σ_{q_j}, represents a reasonable estimate of the resolution of the method. Thus, the pixels showing smaller resolution are associated with higher errors and vice versa.

Resolution at the jth pixel is thus given by

$$R_j = \sqrt{\frac{(\sum_i w_{ij})^2}{\sum_i w_{ij}^2}} \quad \text{(B3)}$$

eq. (B2) can be usefully used to estimate the standard deviation associated with the Q-coda estimated in the single pixel. In this procedure, $\sigma_{Q_{cj}}$ may result apparently small even for small R_j, but this may be due to the data scarcity in that jth pixel, and the estimate may be strongly changed by adding more data. On the contrary, the estimates of σ_{qj} are relatively stable in pixels characterized by high R_j .

We applied eq. (B2) to the present values. σ_i values were estimated from the best fit of the coda envelopes to the single-scattering model (Sato *et al.* 2012). The values of standard deviations of Q_c, $\sigma_{Q_{cj}}$, associated with the any single jth pixel, resulted to be in the interval between 0.1 and 5 (see Fig. 7). This is the reason why in the plots of Figs 4, 5 and 6 we used an interval of 10.0 between adjacent isolines, greater than twice the maximum uncertainty.